Science Advances
AAAS

Supplementary Materials for

An elastomer with ultrahigh strain-induced crystallization

Chase M. Hartquist *et al.*

Corresponding author: Xuanhe Zhao, zhaox@mit.edu; Michael Rubinstein, michael.rubinstein@duke.edu

Sci. Adv. **9**, eadj0411 (2023)
DOI: 10.1126/sciadv.adj0411

This PDF file includes:

Supplementary Text
Figs. S1 to S24
Tables S1 to S4
References

Supplementary Text

Molecular dynamics simulations

In this work, coarse-grained molecular dynamic (CGMD) simulations were used to study polymer chain conformations in the DELSE and in the DELE when crosslinked at the overlap concentration. Although all-atom molecular dynamic simulations are commonly used to study polymer conformations, the small timesteps, many pair interactions, and large polymer chain relaxation times make it challenging to study large systems with entanglements. CGMD groups atoms into beads to improve computational efficiency by reducing the number of degrees of freedom (*49*). CGMD have been used to understand the mechanical and fracture properties of ideal-networks (*50–52*), crystalline polymers (*53*), and elastomers (*54*). There is currently no simulation study comparing polymer chain statistics of DELSE and DELE crosslinked at their overlap concentrations.

The Kremer-Grest (KG) polymer model with added chain rigidity was used to model polymer chain conformations (*55*). Polymers were modeled as repulsive Lennard-Jones (LJ) beads connected by finite extensible nonlinear (FENE) springs. The LJ potential was truncated at the potential minimum and shifted. This LJ potential is also known as the Weeks-Chandler-Anderson (WCA) potential (*56*).

$$U_{\mathrm{WCA}}(r) = \begin{cases} 4\epsilon\left[\left(\frac{\sigma}{r}\right)^{12} - \left(\frac{\sigma}{r}\right)^{6} + \frac{1}{4}\right], & r < 2^{1/6}\sigma \\ 0, & r \geq 2^{1/6}\sigma \end{cases} \quad \text{(S1)}$$

$$U_{\mathrm{FENE}}(r) = -\frac{K}{2}R_0^2 \ln\left[1 - \left(\frac{r}{R_0}\right)^2\right] \quad \text{(S2)}$$

where σ characterizes the bead diameter, ϵ characterizes the repulsive potential energy, K characterizes the spring stiffness, and R_0 characterizes the maximum extension of the spring. Standard parameters were used where $R_0 = 1.5\sigma$, $\epsilon = k_{\mathrm{B}}T$, and $K = 30k_{\mathrm{B}}T$. Angle bending potentials were added to the KG model to introduce stiffness into the polymer backbone, which influence the system's dynamics and structure (*57–59*). An angle bending potential was also added to match the polymer chain stiffness to the properties of PEG (*60*). The angle bending potential is,

$$U_{\mathrm{BEND}}(\theta) = \frac{\kappa}{2}[1 - \cos(\theta)] \quad \text{(S3)}$$

where κ characterizes the bending stiffness. The terms were set to $\kappa = 2.172k_{\mathrm{B}}T$. This potential gives a conversion of roughly 2.56 beads per Kuhn segment.

All simulations were conducted in reduced LJ units with a timestep of $\mathrm{d}t = 0.005\tau^*$ where $\tau^* = t\sqrt{\frac{\epsilon}{m\sigma^2}}$ for mass m. Periodic boundary conditions were used in each direction. Polymer chain lengths of 20, 60, 100, 140, 180, and 220 beads between crosslinking points inclusive were studied in these simulations. Every bead has the same reduced mass of $m^* = 1$. All simulations were conducted in implicit solvent by using the Langevin thermostat with a damping constant of τ^*. All simulations were conducted using the LAMMPS software (*61*) and Moltemplate was used to prepare the simulation data files (*62*).

Initially, a single macromer or chain for each polymer size was simulated in a large simulation box for $10{,}000\tau^*$ to generate a starting configuration. Afterwards, the final configuration of each polymer was randomly inserted using Packmol (*63*) at a very low-density initial state of 0.002. 4 independent configurations were generated this way for each polymer size to obtain better chain statistics when averaged. 32 type-A tetra-arm macromers and 32 type-B tetra-arm macromers were

used to simulate the crosslinked DELSE elastomer in each simulation. Type-A and type-B macromers were differentiated by the bead type at the end of each arm to replicate experimental crosslinking procedures. To ensure that there were about the same number of chains in the crosslinked DELE elastomer simulations, 129 polymer chains were simulated with 86 crosslinking beads. All bead types shared the same chemical and physical properties described above. The only difference between beads was whether they were allowed to react with each other in the crosslinking scheme described below. To sample the unperturbed radius of gyration of each polymer, $500{,}000\tau^*$ were simulated, and the radius of gyrations of all molecules were collected in the final $150{,}000\tau^*$ periodically (see tables S2 and S3). The overlap concentration was then calculated by estimating the averaged pervaded sphere of each molecule using the system averaged radius of gyration.

Each of the samples were then compressed to the overlap concentration using the following scheme based on a procedure from Asai et al. (*63*). First, the simulation volume was reduced by 1% of its initial volume in an isotropic manner over $5{,}000\tau^*$ and then allowed to relax for $50{,}000\tau^*$ to re-equilibrate itself. These two steps were cycled until the overlap concentration was reached. The ratio of initial to overlap volume ranges from about 194 for the shortest chain simulations to about 19 for the longest chains and takes 95 to 99 cycles. Upon reaching the overlap concentration, the polymer solution was equilibrated over $500{,}000\tau^*$. The mean squared displacement and radius of gyration were tracked to ensure that there was sufficient time for the polymers to diffuse distances many times larger than its beyond their radii of gyration and that the system average radius of gyration did not change with time.

Afterwards, the equilibrated system was subjected to a crosslinking procedure using the fix bond/react scheme for up to $1{,}500{,}000\tau^*$ (*64*, *65*). Two dangling chains were allowed to react if they were within a reduced distance of $2^{1/6}$ of each other and satisfied the reaction topology maps. For the DELSE simulations, the reaction topology map was satisfied if a dangling type A and a dangling type B bead were close enough. For the DELE simulations, the reaction topology map was satisfied if a dangling chain end was close enough to a crosslinking bead with less than 3 chains bonded to it. After a reaction, the system's topology between the bonding beads was updated to match the bonding terms described above. Smaller chain length simulations typically had 100% reactions completed while longer chain length simulations had 1 to 2 unreacted chains at the end of this procedure (see table S4).

The crosslinked systems were then deswollen by reducing the volume by 10% of its overlap concentration volume in an isotropic manner over $5{,}000\tau^*$ and then relaxed for $50{,}000\tau^*$. This cycle was looped between 5 and 9 times (depending on overlap concentration volume) until it reached its final equilibrium density of 0.85. The system was then equilibrated for $1{,}000{,}000\tau^*$ while monitoring the system average chain lengths, temperature, and potential energy per bead to ensure equilibration. A production run was conducted for $1{,}000{,}000\tau^*$ with chain statistics output every $50\tau^*$. Unreacted chains and self-looping chains in the DELE were not included in the chain statistic calculations.

For the melt simulations, a procedure based on Auhl et al. was used (*66*). A single polymer chain was simulated in a large simulation box for $10{,}000\tau^*$ to generate a starting configuration. Afterwards, the final configuration of each polymer was randomly inserted using Packmol (*63*) at the final density of 0.85. Instead of using the WCA repulsive term initially, a soft potential was used to remove overlaps between beads.

$$U_{\text{soft}}(r) = \begin{cases} A[1 + \cos\left(\frac{\pi r}{r_c}\right), & r < 2^{1/6}\sigma \\ 0, & r \geq 2^{1/6}\sigma \end{cases} \quad \text{(S4)}$$

where r_c was set to $2^{1/6}\sigma$. The coefficient, A, was linearly ramped from $A = 2\epsilon$ to $A = 100\epsilon$ over $500\tau^*$. The damping coefficient of the Langevin thermostat was set to $\tau^*/4$ to induce stronger coupling to the thermostat. Every $6.25\tau^*$, the velocities of all beads were reset to 0 to promote fast push-offs between overlapping beads. After this initial equilibration, the soft potential was replaced with the original force field and equilibrated for $1{,}000{,}000\tau^*$ with a thermostat damping coefficient set to τ^*. Statistics were then collected in the final production run over an additional $1{,}000{,}000\tau^*$ like the crosslinked simulations described above. All melt statistics were also averaged over 4 independent runs.

Theoretical calculation of the stretch limit of a deswollen end-linked star elastomer

The Arruda-Boyce model gives a means of relating the stretch of a single polymer chain to that of the bulk material (*67*). Here we derive a similar relation for a model of the DELSE. The result indicates that the stretchability of the bulk relates the that of single polymer chains using the following relation:

$$\lambda_1^{\max} \approx \sqrt{3}\lambda_{\text{chain}}/A \quad \text{(S5)}$$

where $\lambda_1^{\max}$ is the maximum bulk stretch, A is a geometric constant, and λ_{chain} is the average maximum single-chain stretch (fig. S19, A-C). This model was used for comparison with the experimental stretch limit (Fig. 4).

Deswollen polymer chain end-to-end distance

The DELSE is crosslinked at the overlap concentration, so the initial volume fraction of polymer can be defined.

$$\phi_0 = \phi^* \quad \text{(S6)}$$

where ϕ_0 is the polymer volume fraction of the end-linked star hydrogel as prepared, and ϕ^* is the overlap volume fraction, which can be written generally as follows.

$$\phi^* = \frac{N v_{\text{mon}}}{V} \approx \frac{N v_{\text{mon}}}{R_0^3} \quad \text{(S7)}$$

where N is the degree of polymerization of a single polymer chain, v_{mon} is the Kuhn monomer volume, V is the volume of polymer chains, and R_0 is the polymer chain end-to-end distance at the overlap concentration, which can be further described as follows.

$$R_0 \approx bN^{\nu} \quad \text{(S8)}$$

where b is the length of a single Kuhn monomer and ν is the pervaded volume (ν = 1/2 for theta solvent while ν = 0.588 for good solvent). The network is then assumed to affinely deswell to the dry state (*44*).

$$\lambda_{\text{d}} = \left(\frac{\phi_{\text{i}}}{\phi_{\text{f}}}\right)^{1/3} \quad \text{(S9)}$$

where λ_{d} is the stretch to deswell from the initial concentration ϕ_{i} to the final concentration ϕ_{f}. For the fully deswollen case of ϕ = 1, the stretch to deswell can be defined for this network.

$$\lambda_{\text{d}} = \phi^{*1/3} \approx \frac{N v_{\text{mon}}}{R_0^3}^{1/3} \approx \left(\frac{v_{\text{mon}}}{b^3}\right)^{1/3} N^{\frac{1-3\nu}{3}} \quad \text{(S10)}$$

The final polymer RMS end-to-end distance can then be determined.

$$\sqrt{R^2} = \sqrt{(\lambda R_0)^2} \approx v_{\text{mon}}^{1/3} N^{1/3} \tag{S11}$$

where R is the end-to-end distance of a single polymer chain in the fully deswollen case. Note that this relation is independent of solvent quality given that gelation occurs at the overlap condition.

Stretch of a single polymer chain

To determine the stretch of a single polymer chain at its elastic, we now must consider the length of a single polymer chain at the elastic limit. This can be written as follows:

$$L = Nb \tag{S12}$$

where L is the length of a fully stretched polymer chain. Note that the finite but small stretching between individual bonds near failure is neglected. We can determine the single chain stretch λ_{chain} using the initial and final lengths defined above.

$$\lambda_{\text{chain}} = \frac{L}{R} \approx \frac{Nb}{v_{\text{mon}}^{1/3} N^{1/3}} = \frac{N^{2/3}}{A} \tag{S13}$$

where A is a constant depending on Kuhn monomer geometry.

Stretch of the bulk material

The bulk material stretch can be approximated as a network of single polymer chains within repeating unit cells. Given an arbitrary deformation to the unit cell (fig. S19, A-C), the average stretch of a single polymer chain can be found through geometrical relations. The characteristic side length of the unit cell is proportional to that of a single polymer chain.

$$a_0 = \frac{4}{\sqrt{3}} R \tag{S14}$$

When the unit cell is stretched, the length of each side is stretched by λ_1, λ_2, and λ_3 in the $\hat{\imath}$, $\hat{\jmath}$, and $\hat{k}$ directions, respectively. A vector representing a single chain can be written as follows:

$$c_{\text{l}} = \frac{a_0}{4}\lambda_1 \hat{\imath} + \frac{a_0}{4}\lambda_2 \hat{\jmath} + \frac{a_0}{4}\lambda_3 \hat{k} \tag{S15}$$

where c_{l} is the vector representing the end-to-end distance and direction of a single polymer chain. The length of this single representative chain in the deformed configuration is given by:

$$R_{\text{chain}} = \frac{a_0}{4}\sqrt{\lambda_1^2 + \lambda_2^2 + \lambda_3^2} \tag{S16}$$

where r_{chain} is the length of a single deformed polymer chain. The length of a single polymer chain can be substituted into this relation.

$$R_{\text{chain}} = \frac{R}{\sqrt{3}}\sqrt{\lambda_1^2 + \lambda_2^2 + \lambda_3^2} \tag{S17}$$

The stretch of a single chain can then be defined in terms of the bulk material stretches.

$$\lambda_{\text{chain}} = \frac{R_{\text{chain}}}{R} = \frac{1}{\sqrt{3}}\sqrt{\lambda_1^2 + \lambda_2^2 + \lambda_3^2} \tag{S18}$$

Using the relation for chain stretch from before, the bulk stretches relate to the number and size of monomers in a single polymer chain.

$$\frac{N^{2/3}}{A} \approx \frac{1}{\sqrt{3}}\sqrt{\lambda_1^2 + \lambda_2^2 + \lambda_3^2} \tag{S19}$$

Experimental conditions

Uniaxial tension and pure shear experimental loading conditions give specific relations for each principal stretch. First, we get the following relation from the incompressibility condition commonly used for rubbers.

$$\lambda_1\lambda_2\lambda_3 = 1 \tag{S20}$$

Measuring using pure shear gives the following principal stretches.

$$\lambda_1 = \lambda, \quad \lambda_2 = \lambda^{-1}, \quad \lambda_3 = 1 \tag{S21}$$

In contrast, uniaxial tension gives the following principal stretches.

$$\lambda_1 = \lambda, \quad \lambda_2 = \lambda^{-1/2}, \quad \lambda_3 = \lambda^{-1/2} \tag{S22}$$

In either case, for highly stretchable materials, the maximum stretch can be approximated as the stretch in the first principal direction.

$$\lambda \approx \lambda_1^{\max} \tag{S23}$$

We can use this to get a fundamental relation relating the maximum stretch to the number and size of monomers in a single polymer chain.

$$\lambda_1^{\max} \approx \sqrt{3}\lambda_{\text{chain}}/A \tag{S24}$$

Theoretical derivation of adiabatic temperature change

The Helmholtz free energy of DELSE can be given in the general case as

$$\Psi = U - TS \tag{S25}$$

where $U = cT - \chi\rho\Delta H$ is the internal energy, c is volumetric specific heat, T is the temperature [K], χ is the crystallinity, ρ is the density, and ΔH is the latent heat (per unit mass) of crystalline domains. S is the total entropy and contains three parts: $S = S_{\text{crys}} + S_{\text{chain}} + S_{\text{thermal}}$, where $S_{\text{crys}} = -\chi\rho\Delta H/T_{\text{c}}$ is the configurational entropy of crystalline domains with T_{c} as the critical crystallization temperature, $S_{\text{chain}}(\lambda,\chi)$ is the configurational entropy by stretching individual polymer chains (which depends on the stretch λ and crystallinity χ), and $S_{\text{thermal}} = c\ln(T/T_{\text{a}})$ is the thermal entropy with T_{a} as the base temperature experienced by the sample. The Helmholtz free energy can be expanded as follows.

$$\Psi = cT - \chi\rho\Delta H - T[-\chi\rho\Delta H/T_{\text{c}} + S_{\text{chain}}(\lambda,\chi) + c\ln(T/T_{\text{a}})] \tag{S26}$$

The equilibrium crystallinity χ_{eq} can be identified by minimizing the free energy with respect to crystallinity.

$$\left(\frac{1}{T_{\text{c}}} - \frac{1}{T}\right)\rho\Delta H = \frac{\partial S_{\text{chain}}}{\partial\chi} \tag{S27}$$

To calculate the temperature change under adiabatic conditions, we impose the condition of constant entropy.

$$\mathrm{d}S = -\frac{\rho\,\Delta H}{T_{\text{c}}}\mathrm{d}\chi + \frac{\partial S_{\text{chain}}}{\partial\lambda}\,\mathrm{d}\lambda + \frac{\partial S_{\text{chain}}}{\partial\chi} + \frac{c}{T}\mathrm{d}T = 0 \tag{S28}$$

The constant entropy condition (Eq. S28) can then be substituted into the equation for the minimization of free energy (Eq. S27).

$$\frac{c}{T}\mathrm{d}T = \frac{\rho\,\Delta H}{T}\mathrm{d}\chi - \frac{\partial S_{\text{chain}}}{\partial\lambda}\,\mathrm{d}\lambda \tag{S29}$$

The adiabatic temperature change can then be calculated.

$$\Delta\mathrm{T}_{\text{adi}} = \frac{\rho\Delta H}{c}\Delta\chi - \frac{1}{c}T\Delta S_{\text{chain}} \tag{S30}$$

where $\Delta\chi$ is the change in crystallinity due to strain-induced crystallization and ΔS_{chain} is the change in configurational entropy of polymer chains due to stretching. For the DELSE, we assume all chains can be stretched to their extension limit.

$$\Delta S_{\text{chain}} = -\frac{1}{2} n k_{\text{b}} \left(\lambda^2 + \frac{2}{\lambda} - 3\right) \tag{S31}$$

where n is the number of effective rubbery amorphous chains per unit volume. Note that this form is used to approximate the entropy change since it assumes ideal Gaussian chain statistics that do not hold for the DELSE system.

The theoretical elastocaloric temperature change due to strain-induced crystallization and configurational entropy can be approximated as follows.

$$\Delta T_{\text{adi}}^{\text{crys}} = \frac{\rho \Delta H}{c} \Delta\chi \approx 70 \Delta\chi \tag{S32}$$

$$\Delta T_{\text{adi}}^{\text{chain}} = -\frac{1}{c} T \Delta S_{\text{chain}} \approx 5.7 \text{ K} \tag{S33}$$

where the material properties, testing parameters, and constants are defined as follows: $\Delta H = 150$ J/g, $\rho = 1.125 \times 10^6$ g/m^3, $c = 2.4 \times 10^6$ J/m^3, $n = 6 \times 10^{25}$ m^{-3}, $k_{\text{b}} = 1.38 \times 10^{-23}$ J/K, and $\lambda = 10$.

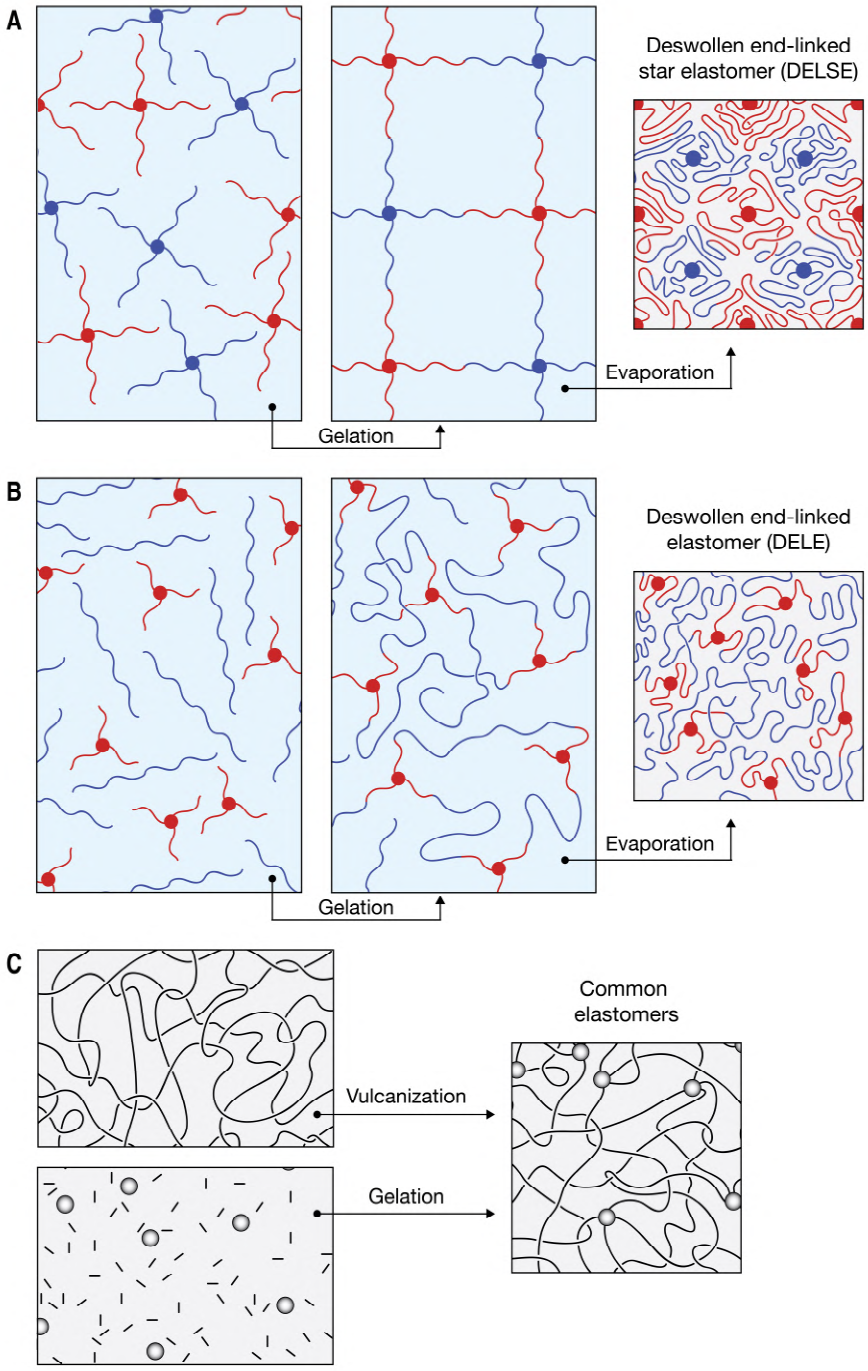


Fig. S1.

Elastomer synthesis. Schematics depict the fabrication process for (**A**) the DELSE, (**B**) the DELE, and (**C**) common elastomers. Illustrations are exaggerated to highlight the differences in network architectures.

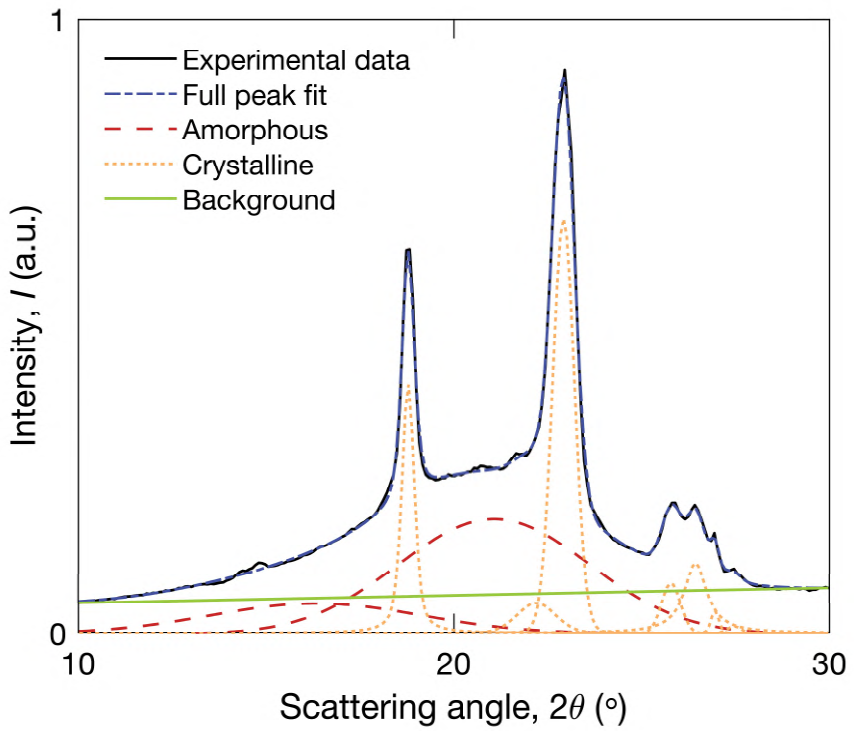


Fig. S2.

1D WAXS curve peak fitting scheme. Crystallinity measurements were classically measured by averaging the 2D WAXS scan over all azimuthal angles to give a single 1D plot. The DELSE was stretched to $0.5\lambda_1^{max}$ to give the representative experimental data.

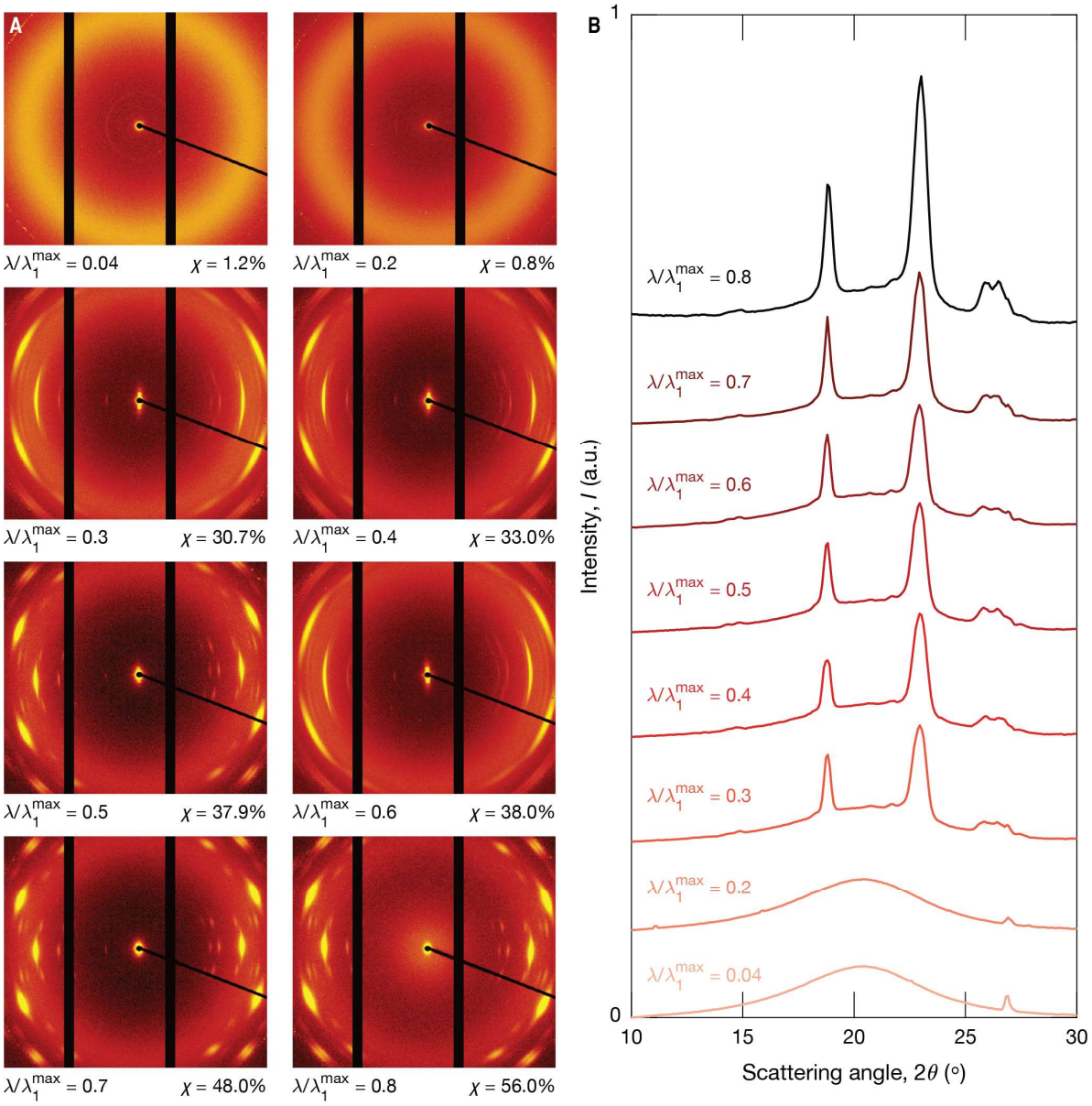


Fig. S3.

DELSE WAXS scans. (**A**) Raw WAXS scans of the DELSE at various stretches are depicted with their measured crystallinity at 55 °C. (**B**) 1D radial WAXS profiles at increasing stretches are averaged over all azimuthal angles.

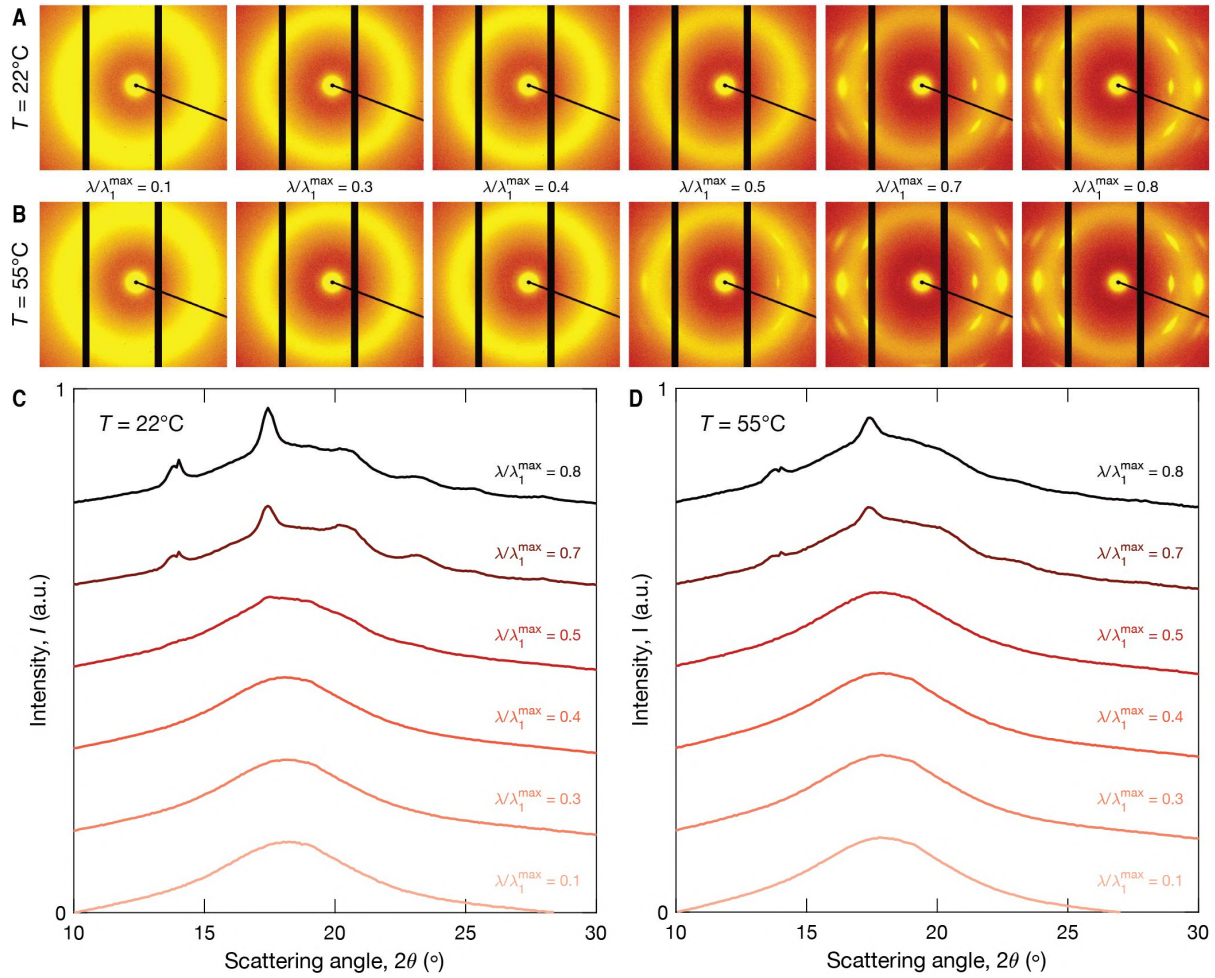


Fig. S4.

NR WAXS scans. (**A**) Raw WAXS scans of NR at various stretches are depicted with their measured crystallinity. 1D radial WAXS profiles at increasing stretches are averaged over all azimuthal angles at (**B**) 22 °C and (**C**) 55 °C.

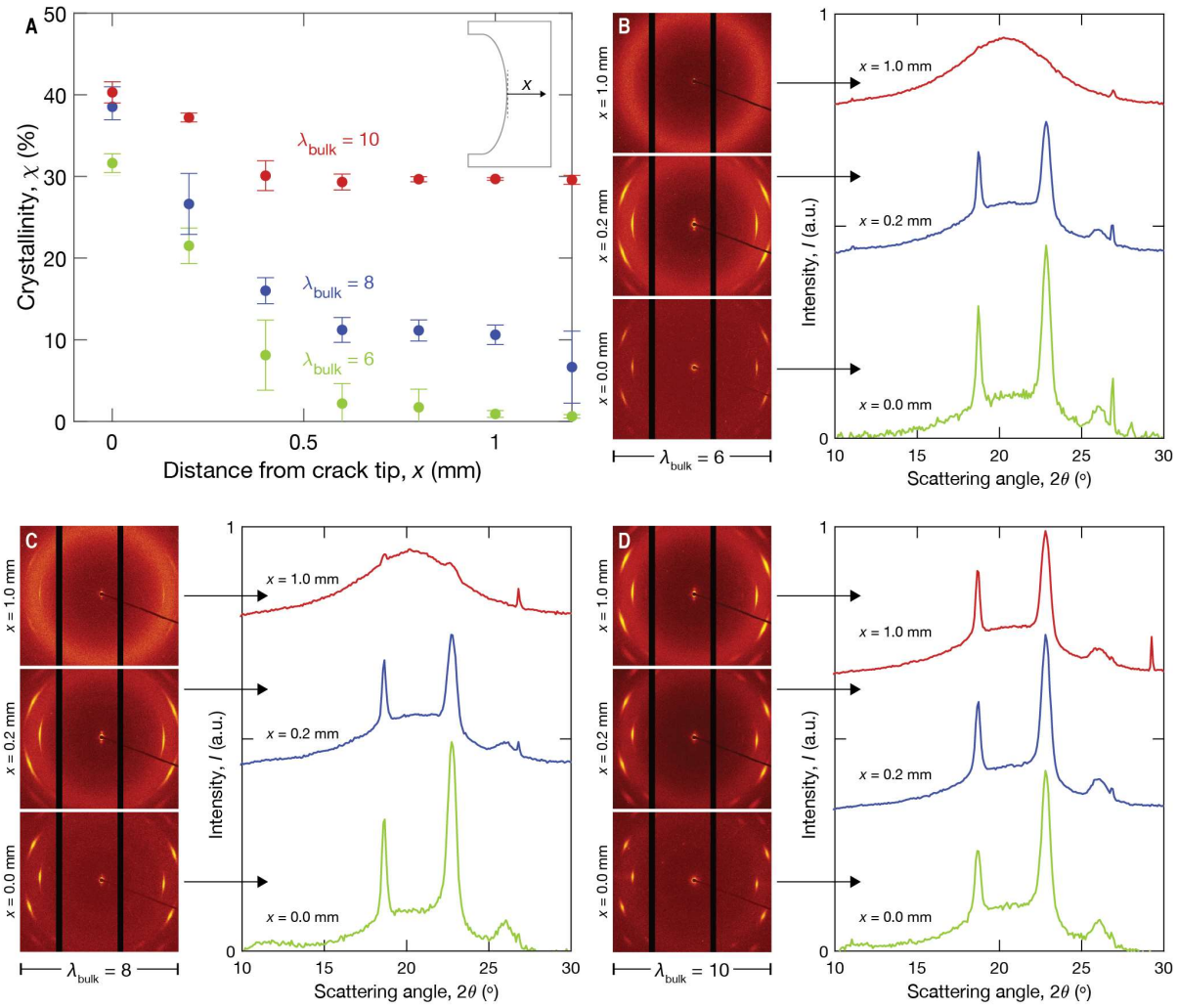


Fig. S5.

Strain-induced crystallization around an artificial notch. (**A**) Strain-induced crystallization heightens around stress concentrations at cracks or flaws in the DELSE at 55 °C. (**B**) At low stretches, the crystallinity increases around the crack while the bulk material remains amorphous. (**C**) At intermediate stretches, the bulk material also develops crystalline domains. (**D**) At high stretches, the crystallinity in the bulk begins to approach that of the crack tip, reinforcing the entire sample.

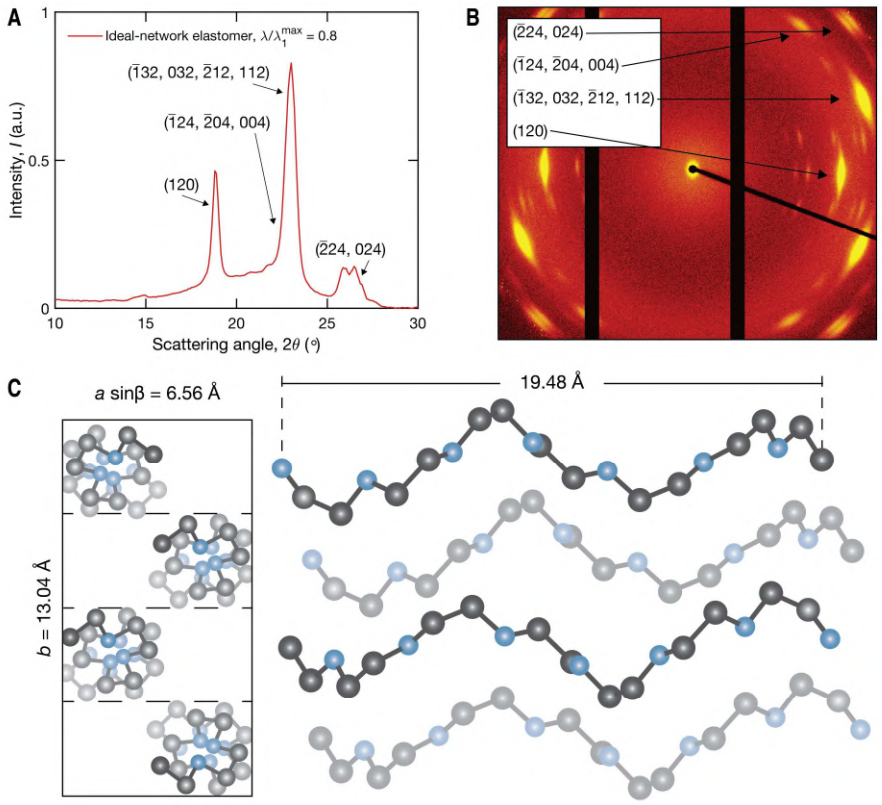


Fig. S6.

(7/2) helical structure of the PEG crystal formed by strain-induced crystallization. (**A**) 1D averaging from WAXS scans over all azimuthal angles for the highly stretched DELSE gives characteristic crystalline peaks associated with PEG crystals, as measured at 55 °C in the stretched configuration. (**B**) The diffraction spots can be labeled the 2D scan. (**C**) The dimensions of the PEG crystal and associated configurations.

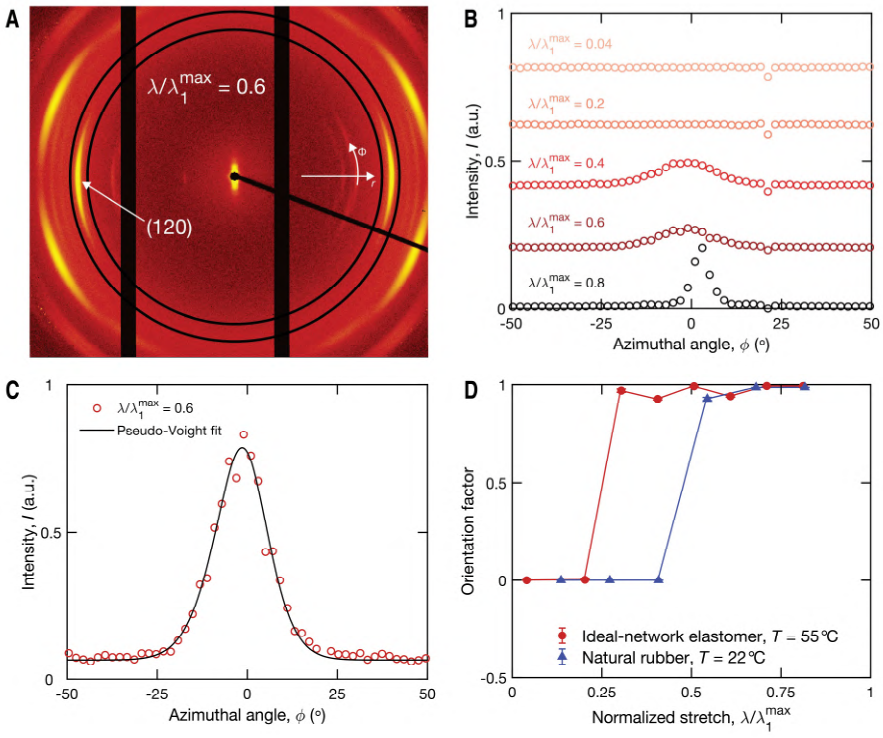


Fig. S7.

Crystallite orientation due to strain-induced crystallization. (**A**) The azimuthal spread of diffraction spots from WAXS scans indicates the degree of crystallite orientation. The (120) peak of the (7/2) helical PEG crystal is studied as a representative of the crystal. (**B**) The azimuthal intensity contribution of the peak spread is captured at increasing stretch at 55 °C. (**C**) Pseudo-Voigt functions fit the azimuthal spread of each peak. (**D**) The Hermans' orientation factor is >0.9 for the DELSE and NR in the regime of strain-induced crystallization, indicating highly oriented crystalline domains in the stretching direction.

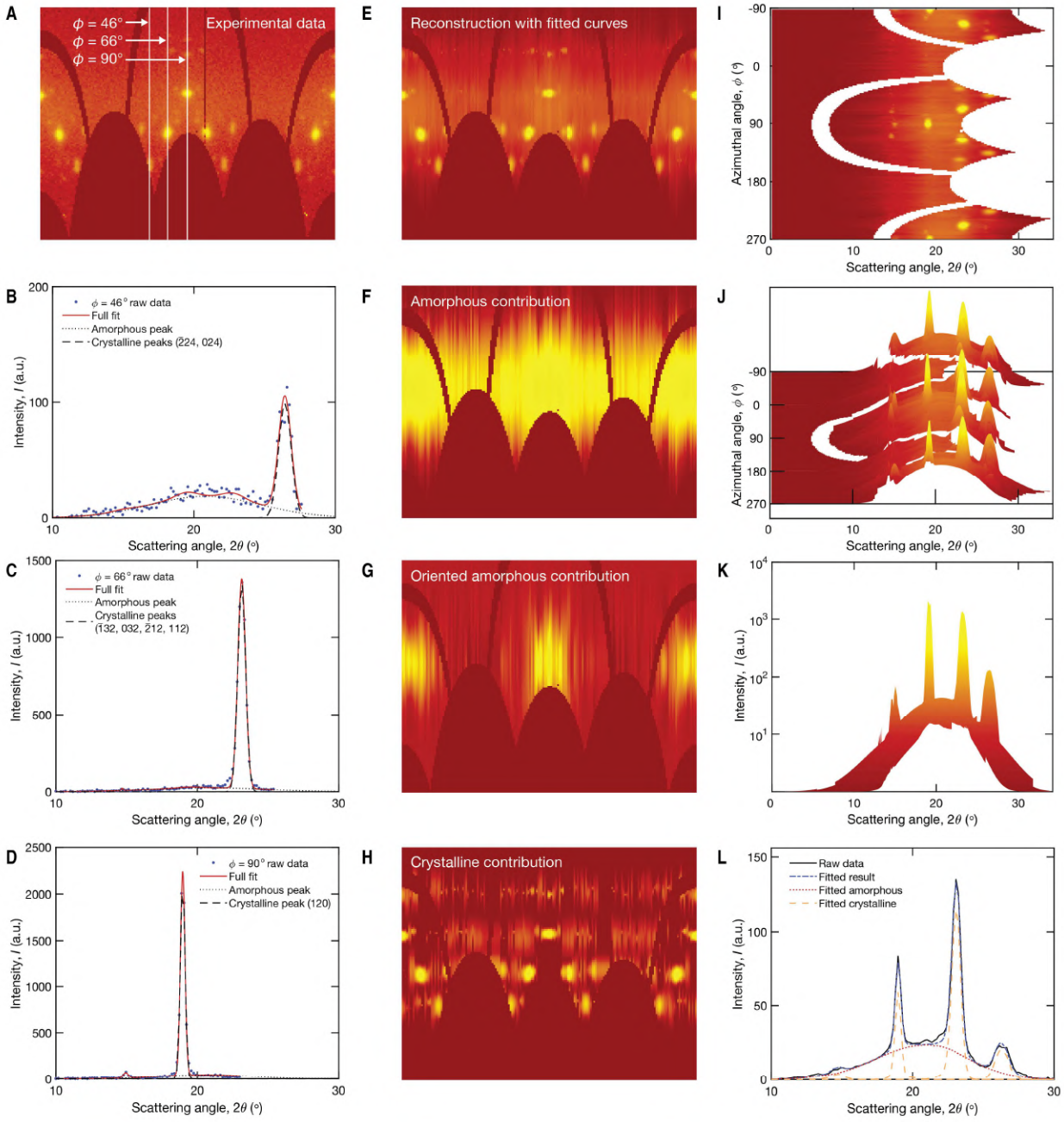


Fig. S8.

Isotropic and anisotropic deconvolution of amorphous and crystalline phases from WAXS patterns. (**A**) Amorphous and crystalline phases from WAXS patterns in polar coordinates are fit with Pseudo-Voigt or Gaussian functions at all azimuthal angles. Representative scans show the crystalline and amorphous diffraction peak contributions at (**B**) 46°, (**C**) 66°, and (**D**) 90°. The fit curves can reconstruct the polar WAXS scan. The (**F**) amorphous, (**G**) oriented amorphous, and (**H**) crystalline contributions can be separated. (**I**) The polar scan shows the intensities of oriented crystals as (**J**) 3D peaks. (**K**) By averaging over all azimuthal angles, the 1D curve depicts how fitting reproduces experimental data. Representative data is shown from the DELSE at 55 °C.

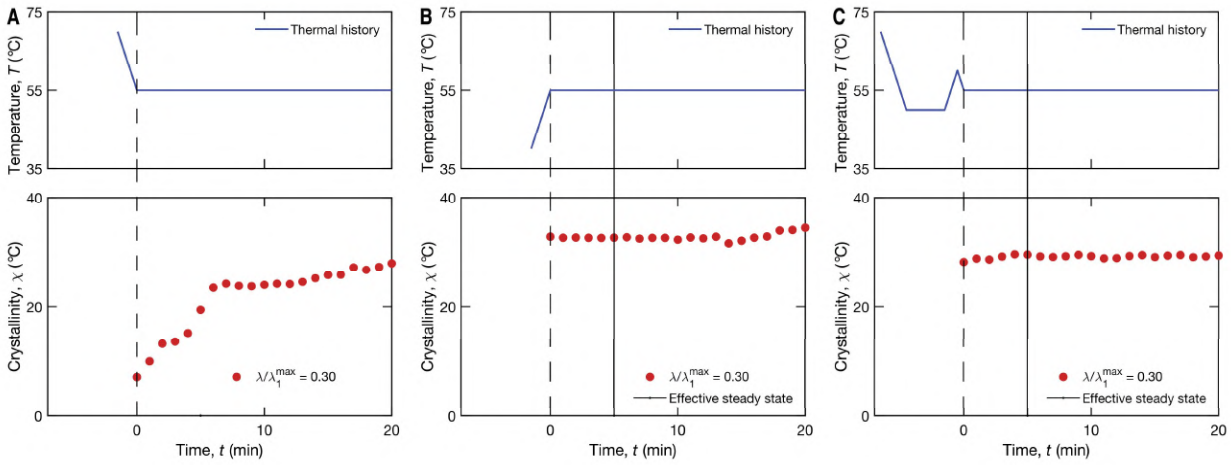


Fig. S9.

Impact of thermal history on strain-induced crystallinity of stretched samples. (**A**) When cooled from high above T_m to 55 °C, the effect of strain-induced crystallization slowly increases with time towards equilibrium. (**B**) When heated from below T_m, the strain-induced crystallization remains relatively constant. (**C**) A more complex thermal history was applied to ensure samples reached an effective steady state before measurement.

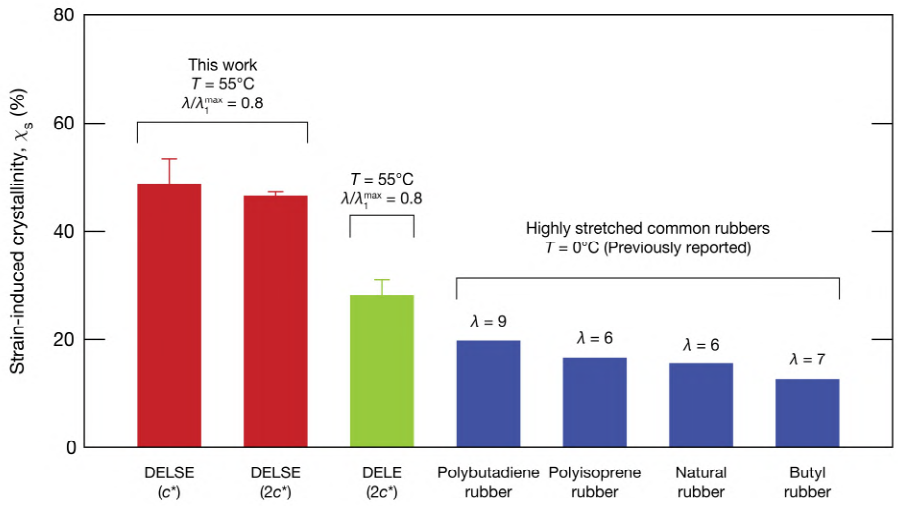


Fig. S10.

Strain-induced crystallinity of the DELSE, DELE, and common rubbers. A direct comparison is included between the DELSE and DELE (T = 55 °C) each prepared at twice their respective overlap concentrations. DELSE and DELE results were measured in this study, while the remaining rubber data is from the literature at 0 °C (*18*).

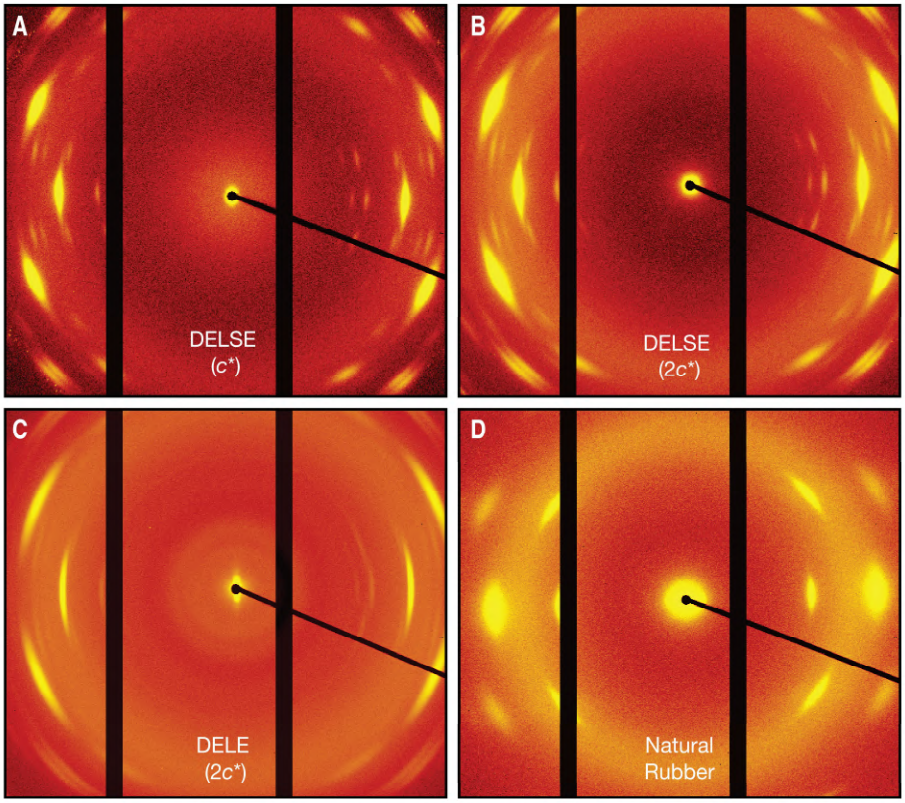


Fig. S11.

WAXS scans of highly stretched elastomers. Raw WAXS scans of (**A**) the DELSE (crosslinked at c^*, T = 55 °C) (**B**) the DELSE (crosslinked at $2c^*$, T = 55 °C), (**C**) the DELE (T = 55 °C), and (**D**) NR (T = 22 °C) stretched to ~$0.8\lambda_1^{\max}$.

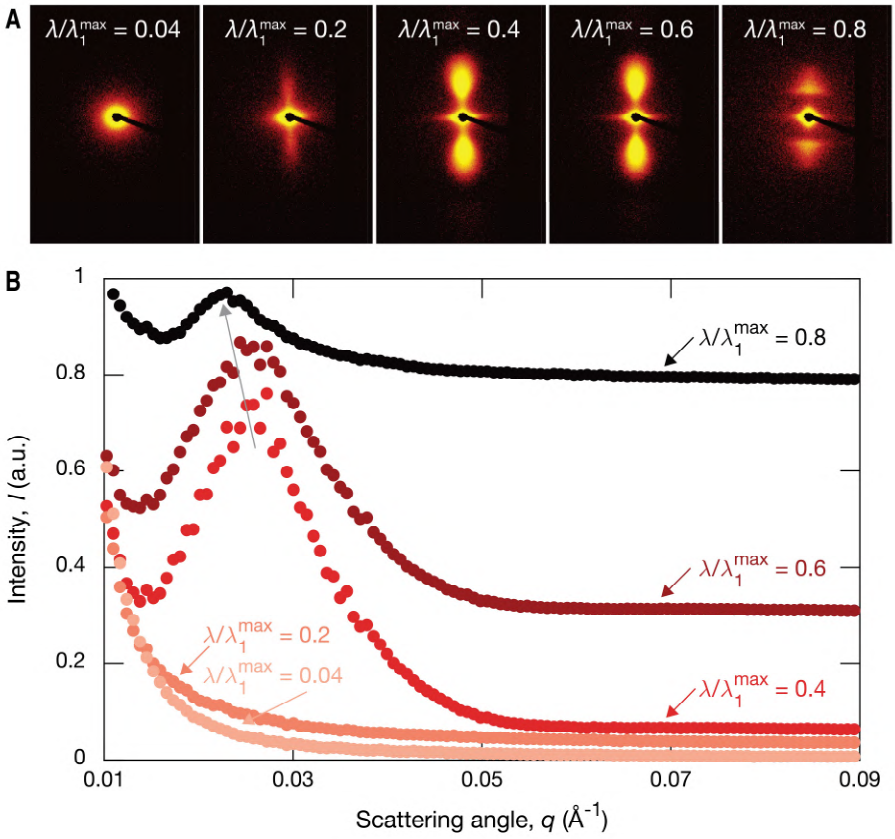


Fig. S12.

Structural transitions during stretching analyzed by SAXS. (**A**) SAXS patterns indicate alignment in the stretching direction of ordered domains of the DELSE at 55 °C. (**B**) The hump in the intensity plots shift to smaller scattering angles at higher stretches, suggesting longer length scales associated with ordered domains.

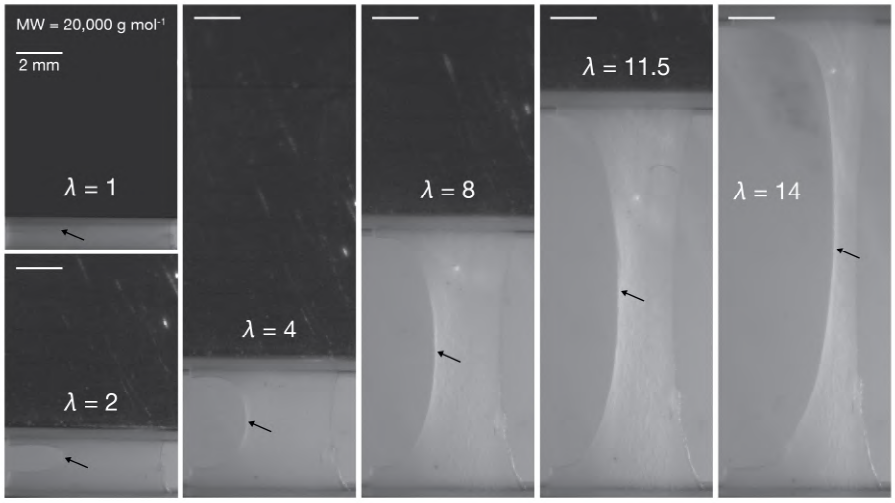


Fig. S13.

Crack propagation through the DELSE with 20,000 g mol^{-1} molecular weight. The fracture toughness was measured to be 4.2 kJ m^{-2} at 60 °C.

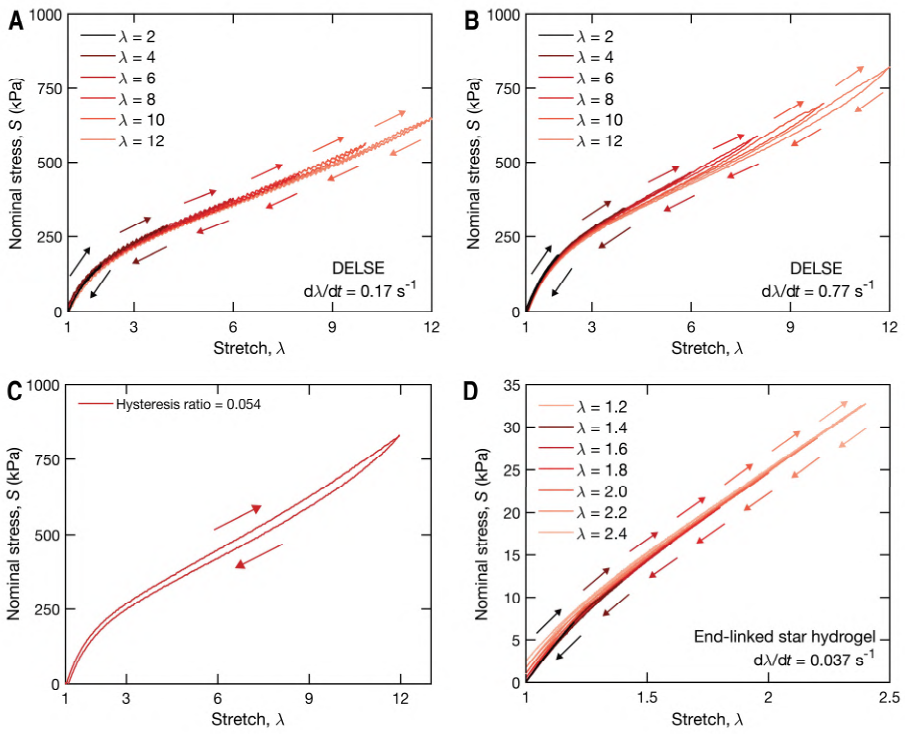


Fig. S14.

Mechanical testing of the DELSE with 10,000 g mol^{-1} molecular weight. Cyclic loading and unloading at (**A**) 0.17 s^{-1} and (**B**) 0.77 s^{-1} shows little hysteresis at 60 °C. (**C**) A single loading and unloading cycle to $\lambda = 12$ gives a hysteresis ratio of 0.054. (**D**) Cyclic hysteresis loops are compared with that of the end-linked star hydrogel at 22 °C.

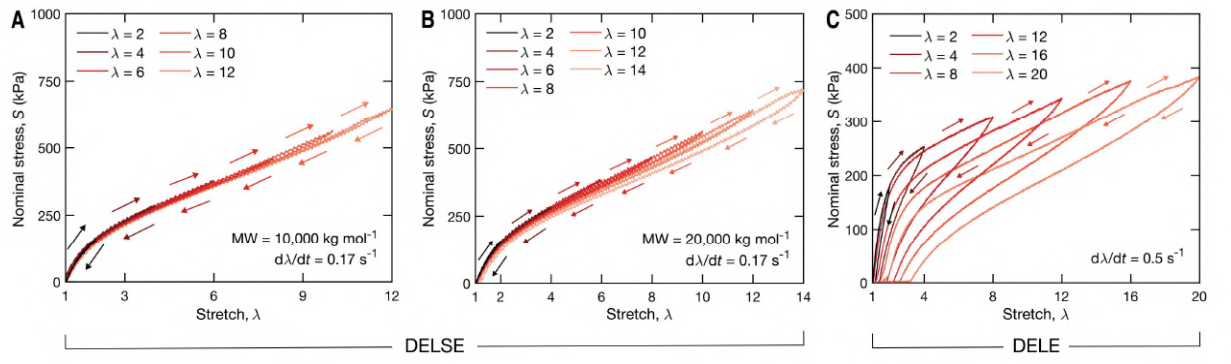


Fig. S15. Mechanical hysteresis of the DELSE and DELE. Cyclic loading and unloading gives low hysteresis for DELSE samples with molecular weights of (**A**) 10,000 g mol^{-1} and (**B**) 20,000 g mol^{-1} yet high hysteresis for (**C**) the DELE sample (T = 60 °C).

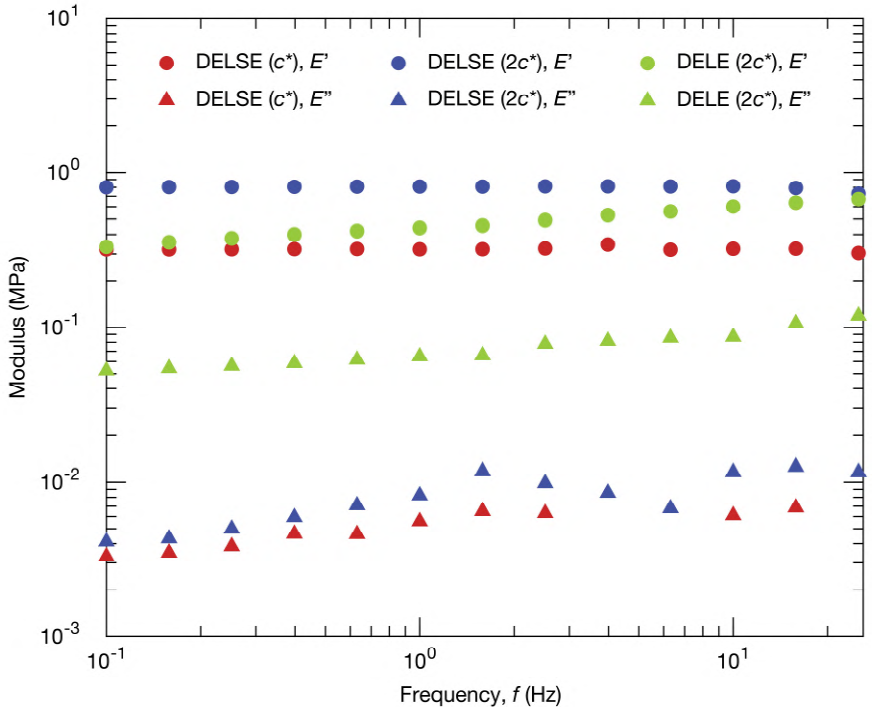


Fig. S16. Dynamic mechanical analysis of the DELSE and DELE. The DELE crosslinked at $2\boldsymbol{c}^*$ is compared with the DELSE crosslinked at c^* and $2c^*$ (T = 60 °C). The DELSE and DELE elastomers have similar storage moduli from 0.1 ~ 10 Hz, but the DELSE exhibits less rate dependence. The loss moduli of both DELSE samples are an order of magnitude smaller than that of the DELE.

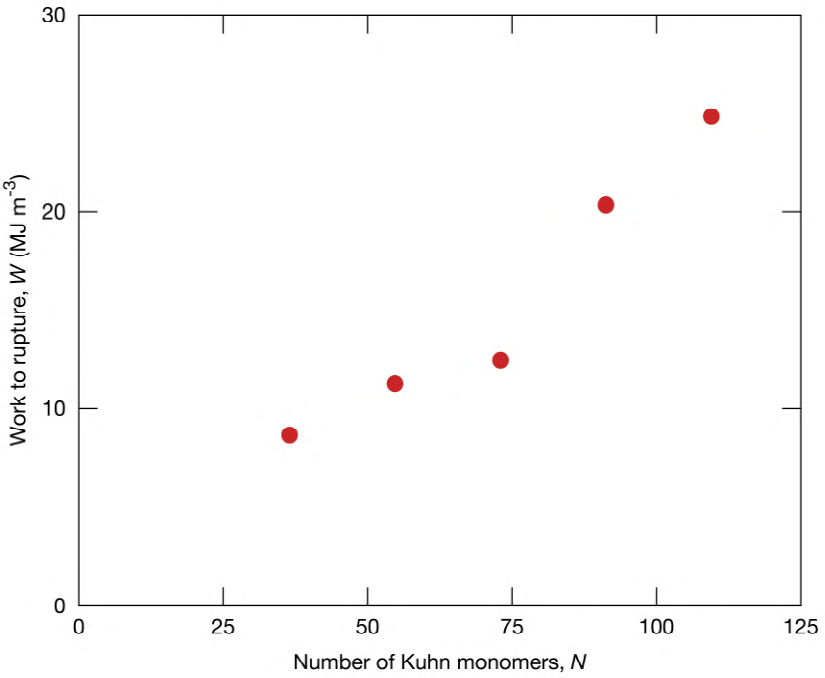


Fig. S17. Work to rupture of the DELSE. Experimental work to rupture measurements at 60 °C with increasing macromer single polymer chain length.

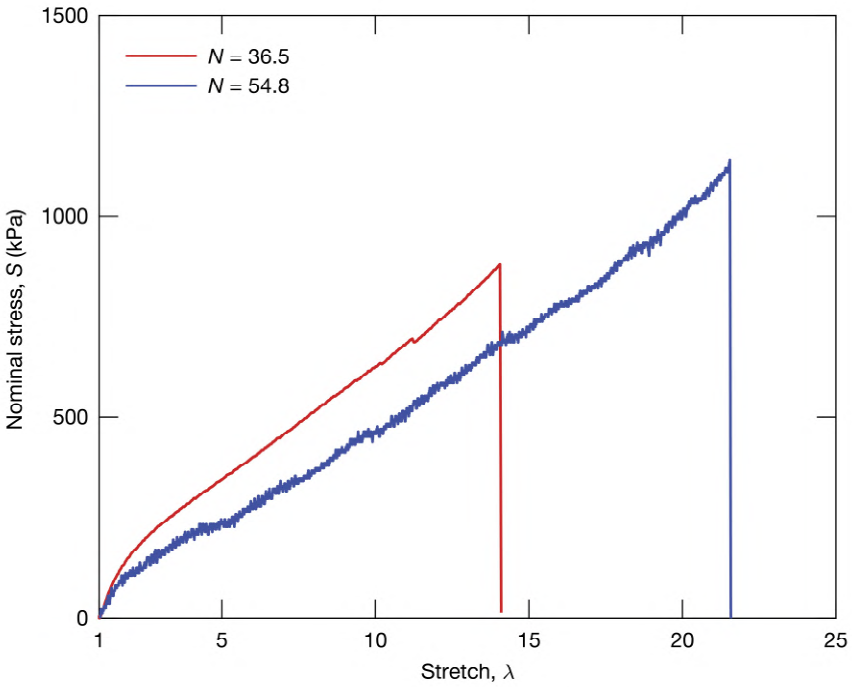


Fig. S18.

Stress-stretch curves are recorded at varying chain lengths. Stretchability of the DELSE elastomer above scales with $N^{2/3}$ (T = 60 °C).

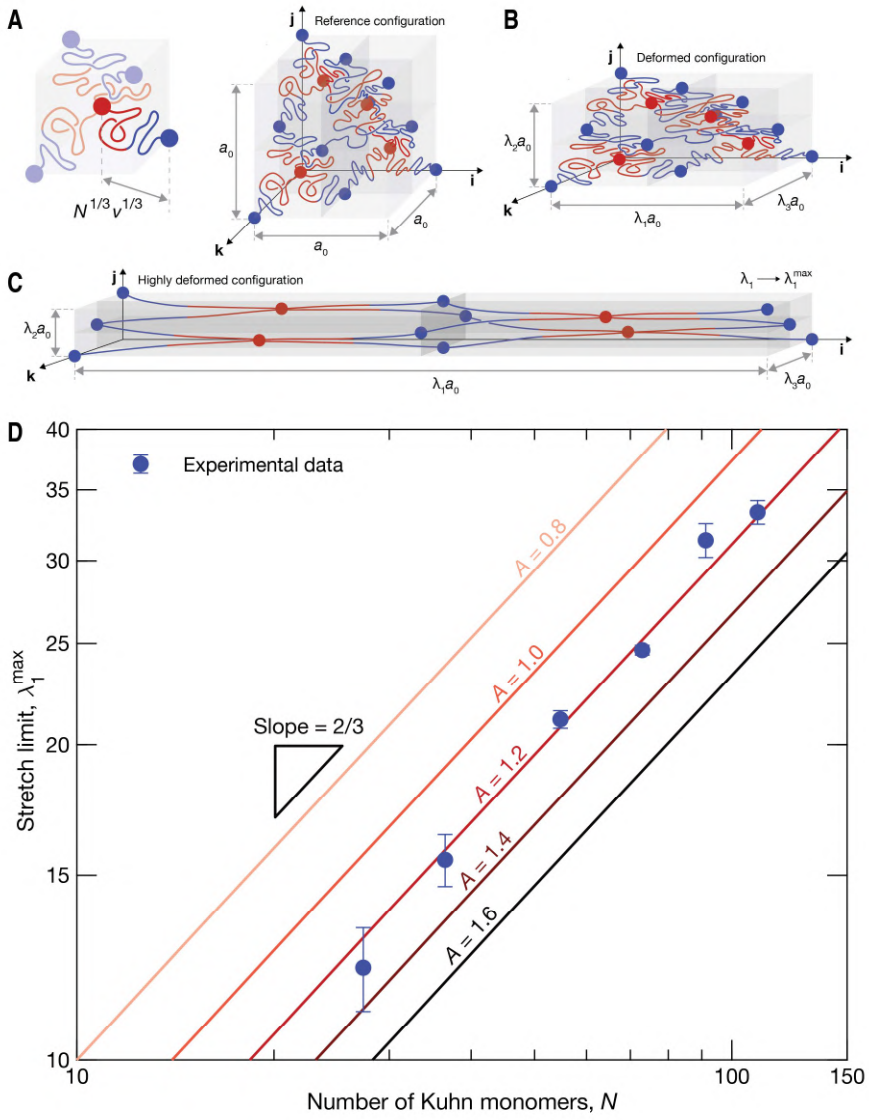


Fig. S19.

Network model for stretchability of the bulk DELSE. (**A**) The microstructural unit cell of the proposed model architecture contains polymer chains whose initial chain length is proportional to $N^{1/3}$. (**B**) Geometric arguments relate the stretchability of the bulk material to that of a single polymer chain. (**C**) Polymer chains align near the elastic stretch limit. (**D**) The effect of changing the geometric variable A is compared to experimental stretchability of the DELSE (T = 60 °C).

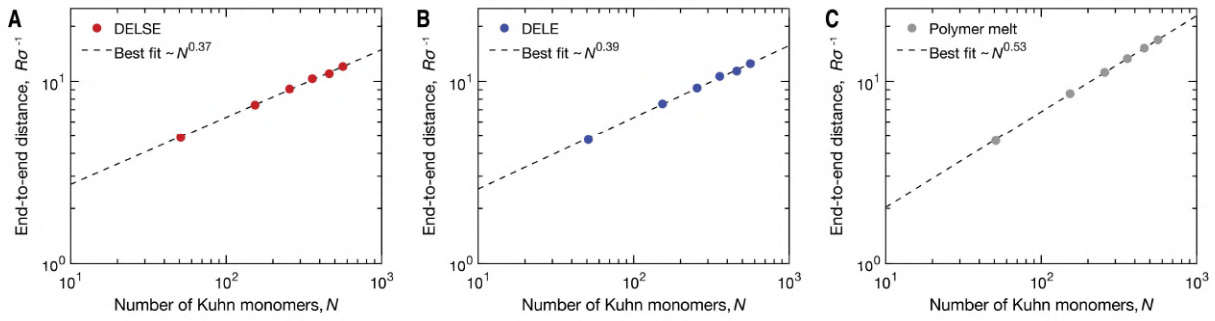


Fig. S20

Molecular dynamics to measure the RMS end-to-end length of polymer chains in networks. The undeformed RMS end-to-end distance of polymer chains within the (**A**) DELSE, (**B**) DELE, and (**C**) a polymer melt scale with $N^{0.37}$, $N^{0.39}$, and $N^{0.53}$, respectively. End-to-end distances are measured from discrete chain snapshots and RMS averaged.

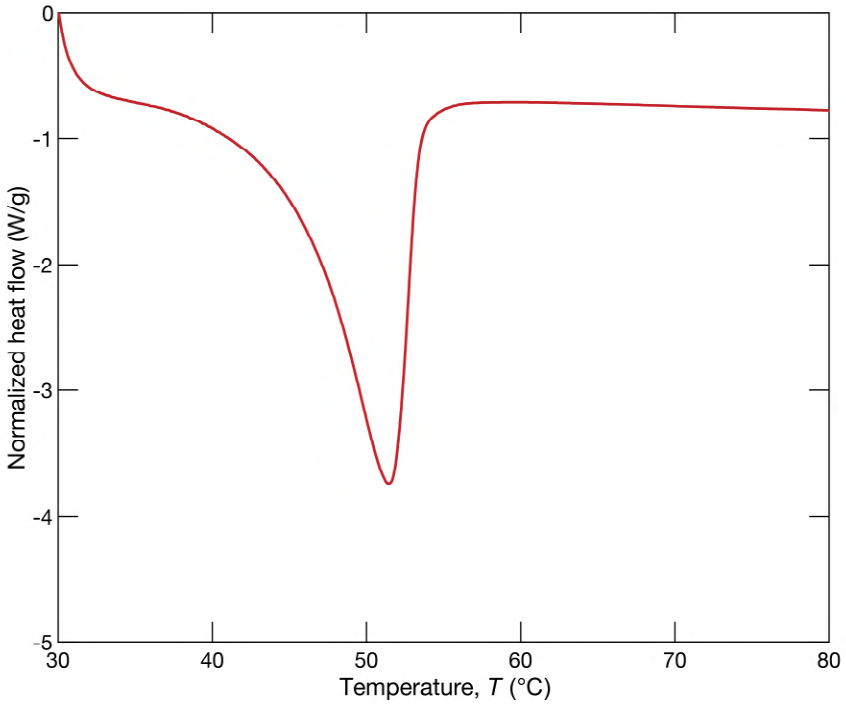


Fig. S21

Differential scanning calorimetry (DSC) of the DELSE. The 20,000 g mol^{-1} molecular weight DELSE measured at a constant heating rate of 10 °C min^{-1} past T_m is depicted.

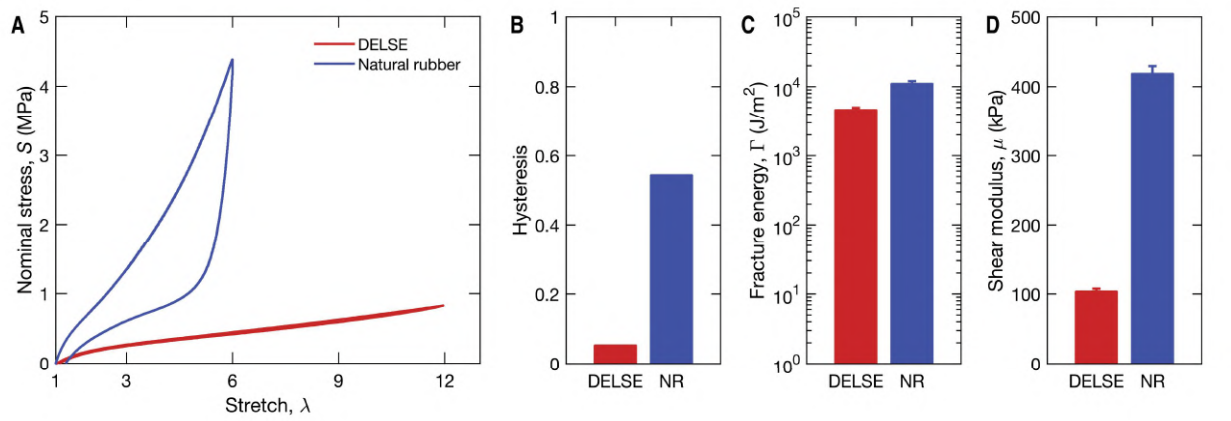


Fig. S22

Mechanical performance comparisons between the DELSE and NR. The (**A**) nominal stress-stretch curves compare loading and unloading of the 10,000 g mol^{-1} DELSE at T = 60 °C to λ = 12 and NR at T = 22 °C to λ = 6; (**B**) hysteresis from this loading cycle is much lower in the DELSE compared with NR. The (**C**) fracture energy of the DELSE at T = 60 °C is on the same order of magnitude as NR from the literature (*45*) while (**D**) the shear modulus – measured using DMA – is significantly lower due to a lower chain density.

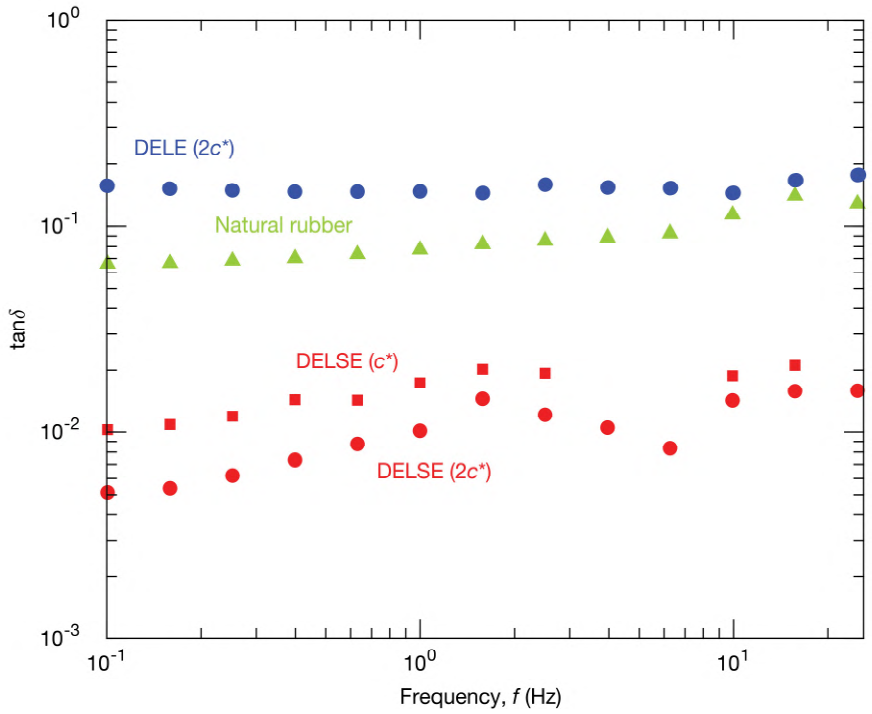


Fig. S23

Loss tangent comparisons between the DELSE, DELE, and NR from DMA. The loss tangent ($\tan\delta = E''/E'$) of the DELSE (T = 60 °C) is about an order of magnitude lower than that of the DELE (T = 60 °C) and NR (T = 25 °C) along a frequency sweep, indicating that the DELSE has fewer defects and that the DELE and NR have a similar defect density.

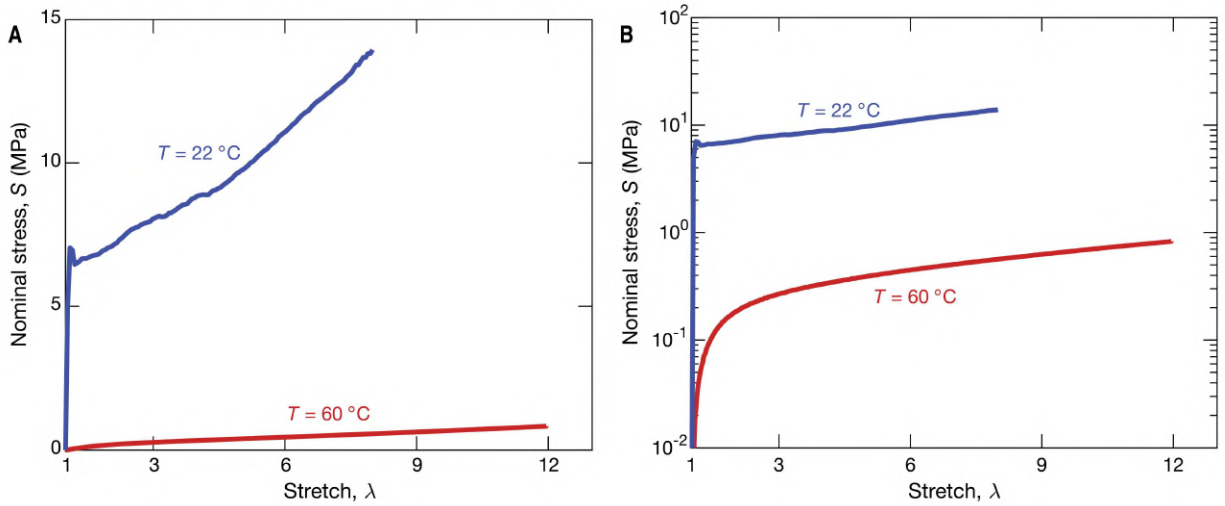


Fig. S24

Mechanical performance of the DELSE above and below the melting temperature. The DELSE with 10,000 g mol^{-1} molecular weight stretched plastically in uniaxial tension below T_m at T = 22 °C to failure is compared with the same material stretched elastically in pure shear above T_m at T = 60 °C on (**A**) linear and (**B**) logarithmic nominal stress scales.

Table S1.
SAXS/WAXS experimental parameters.

Configuration	SAXS	WAXS	WAXS
Measurement	All	Crack tip	All else
Distance from detector (mm)	1059.1 mm	109.1 mm	109.1 mm
Aperture Slit Height	0.7 mm	0.7 mm	0.9 mm
Aperture Slit Width	0.3 mm	0.3 mm	0.9 mm
Wavelength (Å)	1.5409 ($CuK_{\alpha 1}$)	1.5409 ($CuK_{\alpha 1}$)	1.5409 ($CuK_{\alpha 1}$)
Power	45 kV, 0.65 mA	45 kV, 0.65 mA	45 kV, 0.65 mA
Measurement time (s)	180	300	180

Table S2.

Simulated radius of gyration of unreacted polymers for the DELSE.

Arm Length (Beads)	ELSE Macromer Radius of Gyration
9	2.84
29	5.91
49	8.18
69	10.10
89	11.79
109	13.34

Table S3.

Simulated radius of gyration of unreacted polymers for the DELE.

Chain Length (Beads)	DELE Chain Radius of Gyration
18	2.29
58	4.90
98	6.82
138	8.43
178	9.86
218	11.12

Table S4.

Percentage of simulated active chains and self-looping chains (reported as: DELSE% | DELE%).

Chain length	Active chain percentage (%)	Average self-loop percentage (%)
20	100.0 | 95.5	0.0 | 0.4
60	100.0 | 95.3	0.0 | 0.5
100	100.0 | 95.0	0.0 | 0.5
140	99.8 | 92.4	0.0 | 0.7
180	99.6 | 95.0	0.0 | 0.4
220	99.2 | 92.4	0.0 | 0.6

REFERENCES

1. J. R. Katz, X-ray spectrography of polymers and in particular those having a rubber-like extensibility. *Trans. Faraday Soc.* **32**, 77–94 (1936).

2. H. P. Zhang, J. Niemczura, G. Dennis, K. Ravi-Chandar, M. Marder, Toughening effect of strain-induced crystallites in natural rubber. *Phys. Rev. Lett*. 102, 245503 (2009).

3. M. Tosaka, S. Murakami, S. Poompradub, S. Kohjiya, Y. Ikeda, S. Toki, I. Sics, B. S. Hsiao, Orientation and crystallization of natural rubber network as revealed by WAXD using synchrotron radiation. *Macromolecules* **37**, 3299–3309 (2004).

4. S. Toki, T. Fujimaki, M. Okuyama, Strain-induced crystallization of natural rubber as detected real-time by wide-angle X-ray diffraction technique. *Polymer* **41**, 5423–5429 (2000).

5. J. Y. Sun, X. Zhao, W. R. K. Illeperuma, O. Chaudhuri, K. H. Oh, D. J. Mooney, J. J. Vlassak, Z. Suo, Highly stretchable and tough hydrogels. *Nature* **489**, 133–136 (2012).

6. J. P. Gong, Y. Katsuyama, T. Kurokawa, Y. Osada, Double-network hydrogels with extremely high mechanical strength. *Adv. Mater*. **15**, 1155–1158 (2003).

7. E. Ducrot, Y. Chen, M. Bulters, R. P. Sijbesma, C. Creton, Toughening elastomers with sacrificial bonds and watching them break. *Science* **344**, 186–189 (2014).

8. Y. Yang, Z. Song, G. Lu, Q. Zhang, B. Zhang, B. Ni, C. Wang, X. Li, L. Gu, X. Xie, H. Gao, J. Lou, Intrinsic toughening and stable crack propagation in hexagonal boron nitride. *Nature* **594**, 57–61 (2021).

9. E. Filippidi, T. R. Cristiani, C. D. Eisenbach, J. Herbert Waite, J. N. Israelachvili, B. Kollbe Ahn, M. T. Valentine, Toughening elastomers using mussel-inspired iron-catechol complexes. *Science* **358**, 502–505 (2017).

10. N. Domun, H. Hadavinia, T. Zhang, T. Sainsbury, G. H. Liaghat, S. Vahid, Improving the fracture toughness and the strength of epoxy using nanomaterials—A review of the current status. *Nanoscale* **7**, 10294–10329 (2015).

11. J. Kim, G. Zhang, M. Shi, Z. Suo, Fracture, fatigue, and friction of polymers in which entanglements greatly outnumber cross-links. *Science* **374**, 212–216 (2021).

12. C. Liu, N. Morimoto, L. Jiang, S. Kawahara, T. Noritomi, H. Yokoyama, K. Mayumi, K. Ito, Tough hydrogels with rapid self-reinforcement. *Science* **372**, 1078–1081 (2021).

13. T. Fujiyabu, N. Sakumichi, T. Katashima, C. Liu, K. Mayumi, U. Il Chung, T. Sakai, Tri-branched gels: Rubbery materials with the lowest branching factor approach the ideal elastic limit. *Sci. Adv*. **8**, eabk0010 (2022).

14. F. Greibich, R. Schwödiauer, G. Mao, D. Wirthl, M. Drack, R. Baumgartner, A. Kogler, J. Stadlbauer, S. Bauer, N. Arnold, M. Kaltenbrunner, Elastocaloric heat pump with specific cooling power of 20.9 W g^{-1} exploiting snap-through instability and strain-induced crystallization. *Nat. Energy* **6**, 260–267 (2021).

15. S. Zhang, Q. Yang, C. Li, Y. Fu, H. Zhang, Z. Ye, X. Zhou, Q. Li, T. Wang, S. Wang, W. Zhang, C. Xiong, Q. Wang, Solid-state cooling by elastocaloric polymer with uniform chain-lengths. *Nat. Commun.* **13**, 9 (2022).

16. R. Wang, S. Fang, Y. Xiao, E. Gao, N. Jiang, Y. Li, L. Mou, Y. Shen, W. Zhao, S. Li, A. F. Fonseca, D. S. Galvão, M. Chen, W. He, K. Yu, H. Lu, X. Wang, D. Qian, A. E. Aliev, N. Li, C. S. Haines, Z. Liu, J. Mu, Z. Wang, S. Yin, M. D. Lima, B. An, X. Zhou, Z. Liu, R. H. Baughman, Torsional refrigeration by twisted, coiled, and supercoiled fibers. *Science* **366**, 216–221 (2019).

17. C. Lang, E. C. Lloyd, K. E. Matuszewski, Y. Xu, V. Ganesan, R. Huang, M. Kumar, R. J. Hickey, Nanostructured block copolymer muscles. *Nat. Nanotechnol.* **17**, 752–758 (2022).

18. S. Toki, B. S. Hsiao, Nature of strain-induced structures in natural and synthetic rubbers under stretching. *Macromolecules* **36**, 5915–5917 (2003).

19. S. Lin, J. Liu, X. Liu, X. Zhao, Muscle-like fatigue-resistant hydrogels by mechanical training. *Proc. Natl. Acad. Sci. U.S.A.* **116**, 10244–10249 (2019).

20. M. Hua, S. Wu, Y. Ma, Y. Zhao, Z. Chen, I. Frenkel, J. Strzalka, H. Zhou, X. Zhu, X. He, Strong tough hydrogels via the synergy of freeze-casting and salting out. *Nature* **590**, 594–599 (2021).

21. R. B. Dupaix, M. C. Boyce, Finite strain behavior of poly(ethylene terephthalate) (PET) and poly(ethylene terephthalate)-glycol (PETG). *Polymer* **46**, 4827–4838 (2005).

22. X. Liao, M. Dulle, J. M. De Souza E Silva, R. B. Wehrspohn, S. Agarwal, S. Förster, H. Hou, P. Smith, A. Greiner, High strength in combination with high toughness in robust and sustainable polymeric materials. *Science* **366**, 1376–1379 (2019).

23. G. J. Dunderdale, S. J. Davidson, A. J. Ryan, O. O. Mykhaylyk, Flow-induced crystallisation of polymers from aqueous solution. *Nat. Commun.* **11**, 3372 (2020).

24. J. Gough, VII. A description of a property of caoutchouc, or indian rubber; with some reflections on the cause of the elasticity of this substance. In a letter to Dr. Holme. *Philos. Mag.* **24**, 39–43 (1805).

25. T. Sakai, T. Matsunaga, Y. Yamamoto, C. Ito, R. Yoshida, S. Suzuki, N. Sasaki, M. Shibayama, Ung-il Chung, Design and fabrication of a high-strength hydrogel with ideally homogeneous network structure from tetrahedron-like macromonomers. *Macromolecules* **41**, 5379–5384 (2008).

26. Y. Nomoto, T. Matsunaga, T. Sakai, M. Tosaka, M. Shibayama, Structure and physical properties of dried Tetra-PEG gel. *Polymer* **52**, 4123–4128 (2011).

27. T. Yamamoto, J. A. Campbell, S. Panyukov, M. Rubinstein, Scaling theory of swelling and deswelling of polymer networks. *Macromolecules* **55**, 3588–3601 (2022).

28. H. M. James, E. Guth, Theory of the increase in rigidity of rubber during cure. *J. Chem. Phys*. **15**, 669–683 (1947).

29. Y. Akagi, T. Katashima, H. Sakurai, U. Il Chung, T. Sakai, Ultimate elongation of polymer gels with controlled network structure. *RSC Adv*. **3**, 13251–13258 (2013).

30. M. C. Boyce, E. M. Arruda, Constitutive models of rubber elasticity: A review. *Rubber Chem. Technol*. **73**, 504–523 (2000).

31. L. R. G. Treloar, *The Physics of Rubber Elasticity* (Oxford Univ. Press, 1975).

32. S. Lin, J. Ni, D. Zheng, X. Zhao, Fracture and fatigue of ideal polymer networks. *Extreme Mech. Lett*. **48**, 101399 (2021).

33. K. Urayama, S. Kohjiya, Uniaxial elongation of deswollen polydimethylsiloxane networks with supercoiled structure. *Polymer* **38**, 955–962 1997.

34. H. Tadokoro, Y. Chatani, T. Yoshihara, S. Tahara, S. Murahashi, Structural studies on polyethers, [-(CH2)m-O-]n. II. Molecular structure of polyethylene oxide. *Makromol. Chem*. **73**, 109–127 (1964).

35. Y. Takahashi, I. Sumita, H. Tadokoro, Structural studies of polyethers. IX. Planar zigzag modification of poly(ethylene oxide). *J. Polym. Sci. Polym. Phys. Ed.* **11**, 2113–2122 (1973).

36. Y. Takahashi, H. Tadokoro, Structural studies of polyethers, (–(CH2)m–O–)n. X. Crystal structure of poly(ethylene oxide). *Macromolecules* **6**, 672–675 (1973).

37. S. Ran, D. Fang, X. Zong, B. S. Hsiao, B. Chu, P. M. Cunniff, Structural changes during deformation of Kevlar fibers via on-line synchrotron SAXS/WAXD techniques. *Polymer* **42**, 1601–1612 (2001).

38. S. Toki, I. Sics, S. Ran, L. Liu, B. S. Hsiao, S. Murakami, K. Senoo, S. Kohjiya, New insights into structural development in natural rubber during uniaxial deformation by in situ synchrotron X-ray diffraction. *Macromolecules* **35**, 6578–6584 (2002).

39. G. Nian, J. Kim, X. Bao, Z. Suo, Making highly elastic and tough hydrogels from doughs. *Adv. Mater*. **34**, e2206577 (2022).

40. T. Katashima, M. Asai, K. Urayama, U. Il Chung, T. Sakai, Mechanical properties of tetra-PEG gels with supercoiled network structure. *J. Chem. Phys*. **140**, 074902 (2014).

41. Z. Xie, G. Sebald, D. Guyomar, Temperature dependence of the elastocaloric effect in natural rubber. *Phys. Lett. A* **381**, 2112–2116 (2017).

42. Y. Akagi, H. Sakurai, J. P. Gong, U. Il Chung, T. Sakai, Fracture energy of polymer gels with controlled network structures. *J. Chem. Phys.* **139**, 144905 (2013).

43. T. Matsunaga, T. Sakai, Y. Akagi, U. Il Chung, M. Shibayama, Structure characterization of tetra-PEG gel by small-angle neutron scattering. *Macromolecules* **42**, 1344–1351 (2009).

44. M. Rubinstein, R. H. Colby, *Polymer Physics* (Oxford Univ. Press, 2003).

45. R. S. Rivlin, A. G. Thomas, Rupture of rubber. I. Characteristic energy for tearing. *J. Polym. Sci*. **10**, 291–318 (1953).

46. P. J. Flory, M. Volkenstein, *Statistical Mechanics of Chain Molecules* (Interscience Publishers, 1969), pp. 699–700.

47. L. H. Cai, T. E. Kodger, R. E. Guerra, A. F. Pegoraro, M. Rubinstein, D. A. Weitz, Soft poly(dimethylsiloxane) elastomers from architecture-driven entanglement free design. *Adv. Mater*. **27**, 5132–5140 (2015).

48. Z. W. Wilchinsky, Measurement of orientation in polypropylene film. *J. Appl. Phys*. **31**, 1969–1972 (1960).

49. T. E. Gartner, A. Jayaraman, Modeling and simulations of polymers: A roadmap. *Macromolecules* **52**, 755–786 (2019).

50. C. W. Barney, Z. Ye, I. Sacligil, K. R. McLeod, H. Zhang, G. N. Tew, R. A. Riggleman, A. J. Crosby, Fracture of model end-linked networks. *Proc. Natl. Acad. Sci. U.S.A.* **119**, e2112389119 (2022).

51. E. Wang, F. A. Escobedo, Mechanical properties of tetrapolyethylene and tetrapoly(ethylene oxide) diamond networks via molecular dynamics simulations. *Macromolecules* **49**, 2375–2386 (2016).

52. E. Wang, F. Escobedo, Swelling and tensile properties of tetra-polyethylene glycol via coarse-grained molecular models. *Macromol. Theory Simul*. **26**, 1600098 (2017).

53. Y. Higuchi, Fracture processes of crystalline polymers using coarse-grained molecular dynamics simulations. *Polym. J*. **50**, 579–588 (2018).

54. Y. Yin, N. Bertin, Y. Wang, Z. Bao, W. Cai, Topological origin of strain induced damage of multi-network elastomers by bond breaking. *Extreme Mech. Lett*. **40**, 100883 (2020).

55. K. Kremer, G. S. Grest, Dynamics of entangled linear polymer melts: A molecular-dynamics simulation. *J. Chem. Phys*. **92**, 5057–5086 (1990).

56. J. D. Weeks, D. Chandler, H. C. Andersen, Role of repulsive forces in determining the equilibrium structure of simple liquids. *J. Chem. Phys*. **54**, 5237–5247 (1971).

57. R. Faller, A. Kolb, F. Müller-Plathe, Local chain ordering in amorphous polymer melts: Influence of chain stiffness. *Phys. Chem. Chem. Phys*. **1**, 2071–2076 (1999).

58. R. Faller, F. Müller-Plathe, A. Heuer, Local reorientation dynamics of semiflexible polymers in the melt. *Macromolecules* **33**, 6602–6610 (2000).

59. R. Faller, F. Müller-Plathe, Chain stiffness intensifies the reptation characteristics of polymer dynamics in the melt. *ChemPhysChem* **2**, 180–184 (2001).

60. R. Everaers, H. A. Karimi-Varzaneh, F. Fleck, N. Hojdis, C. Svaneborg, Kremer-grest models for commodity polymer melts: Linking theory, experiment, and simulation at the kuhn scale. *Macromolecules* **53**, 1901–1916 (2020).

61. A. P. Thompson, H. M. Aktulga, R. Berger, D. S. Bolintineanu, W. M. Brown, P. S. Crozier, P. J. t'Veld, A. Kohlmeyer, S. G. Moore, T. D. Nguyen, R. Shan, M. J. Stevens, J. Tranchida, C. Trott, S. J. Plimpton, LAMMPS - a flexible simulation tool for particle-based materials modeling at the atomic, meso, and continuum scales. *Comput. Phys. Commun.* **271**, 108171 (2022).

62. A. I. Jewett, D. Stelter, J. Lambert, S. M. Saladi, O. M. Roscioni, M. Ricci, L. Autin, M. Maritan, S. M. Bashusqeh, T. Keyes, R. T. Dame, J. E. Shea, G. J. Jensen, D. S. Goodsell, Moltemplate: A tool for coarse-grained modeling of complex biological matter and soft condensed matter physics. *J. Mol. Biol*. **433**, 166841 (2021).

63. L. Martínez, R. Andrade, E. G. Birgin, J. M. Martínez, PACKMOL: A package for building initial configurations for molecular dynamics simulations. *J. Comput. Chem*. **30**, 2157–2164 (2009).

64. J. R. Gissinger, B. D. Jensen, K. E. Wise, Modeling chemical reactions in classical molecular dynamics simulations. *Polymer* **128**, 211–217 (2017).

65. J. R. Gissinger, B. D. Jensen, K. E. Wise, Reacter: A heuristic method for reactive molecular dynamics. *Macromolecules* **53**, 9953–9961 (2020).

66. R. Auhl, R. Everaers, G. S. Grest, K. Kremer, S. J. Plimpton, Equilibration of long chain polymer melts in computer simulations. *J. Chem. Phys*. **119**, 12718–12728 (2003).

67. E. M. Arruda, M. C. Boyce, A three-dimensional constitutive model for the large stretch behavior of rubber elastic materials. *J. Mech. Phys. Solids* **41**, 389–412 (1993).